# Dalton Transactions

Accepted Manuscript






ROYAL SOCIETY OF CHEMISTRY

www.rsc.org/dalton

# Soft ferromagnetism in mixed valence $Sr_{1-x}La_xTi_{0.5}Mn_{0.5}O_3$ perovskites

Ilyas Qasim, Peter E.R Blanchard, Brendan J. Kennedy*, Chris D. Ling

*School of Chemistry, The University of Sydney, Sydney, NSW 2006, Australia*

Ling-Yun Jang

*Facility Utilization Group, Experiment Facility Division, National Synchrotron Radiation Research Center, Hsinchu 30076, Taiwan*

Takashi Kamiyama, Ping Miao and Shuki Torii

*Institute of Materials Structure Science, High Energy Accelerator Research Organization KEK, Tsukuba, Ibaraki 305-0801, Japan*

* To whom correspondence should be addressed

Brendan J. Kennedy

School of Chemistry

The University of Sydney

Sydney, NSW 2006 AUSTRALIA

Ph +61 2 9351 2742

Fax + 61 2 9351 3329

E-mail. B.Kennedy@chem.usyd.edu.au

## Abstract

The structural, magnetic and electrical properties of the mixed Ti-Mn oxides $Sr_{1-x}La_xTi_{0.5}Mn_{0.5}O_3$ $(0 \le x \le 0.5)$ are reported. At room temperature the oxides have a cubic structure in space group $Pm\bar{3}m$ for $x \le 0.25$ and rhombohedral in $R\bar{3}c$ for $0.3 \le x \le 0.50$. X-ray absorption spectroscopic measurements demonstrate the addition of $La^{3+}$ is compensated by the partial reduction of $Mn^{4+}$ to $Mn^{3+}$. Variable temperature neutron diffraction measurements show that cooling $Sr_{0.6}La_{0.4}Ti_{0.5}Mn_{0.5}O_3$ results in a first order transition from rhombohedra to an orthorhombic structure in *Imma*. Complex magnetic behaviour is observed. The magnetic behaviour of the mixed valent ($Mn^{3+/4+}$) examples is dominated by ferromagnetic interactions, although cation disorder frustrates long range magnetic ordering.

## Introduction

Manganate perovskites of the type $A_{1-x}Ln_xMnO_3$ (*A* alkaline earth, *Ln* lanthanoid,) have long been a subject of interest, as they demonstrate fascinating and technologically relevant electrical and magnetic properties[1-5]. In recent times we have reported on a series of studies of Ce and Pr doped $SrMnO_3$ focusing on the coupling of the lattice, orbital and spin degrees of freedom [6-9]. These studies have revealed a remarkable disjoint between the distortion of the $MnO_6$ octahedra and the unit cell metric. The presence of $Mn^{3+}$ in perovskites can lead to unexpected behaviour as evident by the ferroelectricity (FE) observed in $TbMnO_3$ [10]. Recently there have been reports of the coexistence of FE and ferromagnetism (FM), in addition to a colossal dielectric response, in the Ti substituted oxide $SrTi_{0.5}Mn_{0.5}O_3$ [11, 12]. Co-substitution of both the Sr and Mn in $SrMnO_3$ provides considerable flexibility in tuning these oxides and increases the potential for designing materials for specific applications. Partial replacement of the Sr with trivalent *Ln* cations in $Sr_{1-x}Ln_xTi_{0.5}Mn_{0.5}O_3$ reduces the $Mn^{4+}$ ( $t_{2g}^3\, e_g^0$) ions to $Mn^{3+}$ ( $t_{2g}^3\, e_g^1$), which, in turn, drives structural and electronic changes. Since the oxidation state is one of the key factors affecting structure and properties in manganate perovskites, this potentially enables researchers tune the properties to desired functionalities. This approach has been explored by Álvarez-Serrano and co-workers who observed complex magnetic behaviour in the relaxor manganites $Sr_{2-x}Bi_xTiMnO_6$. They showed the materials to be magnetically frustrated as a consequence of the disorder of the Mn cations, although the higher than expected magnetic moments indicated the presence of FM clusters[13].

A lack of consensus both on structure and magnetism is a distinct feature of existing literature on $Sr_{1-x}A_xTi_{0.5}Mn_{0.5}O_3$ type materials[12, 14-18]. Álvarez-Serrano concluded that the Ti and Mn were disordered at the octahedral sites in $Sr_{2-x}Bi_xTiMnO_6$; consequently these are better described as $Sr_{1-x}Bi_xTi_{0.5}Mn_{0.5}O_3$ The same group reported that $Sr_{0.5}La_{0.5}Ti_{0.5}Mn_{0.5}O_3$ has an orthorhombic (*Pbnm*) structure, and that it displayed ferromagnetism despite the lack of long range ordering of the $Mn^{3+}$ and $Ti^{4+}$ cations[16]. Subsequently, Kallel and co-workers described the same material but concluded that the structure was rhombohedral in $R\bar{3}c$, and it was a spin-glass at low temperatures[15]. In our recent report we addressed structural aspects of these La-doped $SrTi_{1/2}Mn_{1/2}O_3$ oxides and established that the end member, $SrMn_{0.5}Ti_{0.5}O_3$, and La doped $Sr_{1-x}A_xTi_{0.5}Mn_{0.5}O_3$ materials with *x* up to 0.25 are cubic in space group $Pm\bar{3}m$; there being no evidence for ordering the $Ti^{4+}$ and $Mn^{4+}$ cations[19]. The

structures of the materials are rhombohedral, in $R\bar{3}c$, when the La-doping amount is further increased[19].

In this paper we describe the magnetic and electrical properties of *A*-site La doped $Sr_{1-x}La_xTi_{0.5}Mn_{0.5}O_3$ solid solution. Neutron diffraction methods have been used to establish precise structures for representative examples, and in particular to examine the possibility of magnetic ordering at low temperatures.

**Experimental**

Seven polycrystalline samples of $Sr_{1-x}La_xTi_{0.5}Mn_{0.5}O_3$ ($x$ = 0, 0.1, 0.2, 0.25, 0.3, 0.4, 0.5) were prepared by a conventional solid-state reaction, using $SrCO_3$, $La_2O_3$, $TiO_2$ and $MnCO_3$ as starting materials. The reagents were finely mixed in an acetone slurry using an agate mortar and pestle before being heated in air at 1000 °C for 12 hours, and 1200 °C for 48 hours with re-grinding and pelletizing before every heating step. After a final re-grinding, the $x$ = 0 and 0.1 samples were heated at 1450°C whereas all other samples were annealed at 1350 °C for 48 hours and then furnace-cooled down to around 100°C at the approximate cooling rate of 4°C/min. All reactions were monitored by powder X-ray diffraction with Cu Kα radiation, using a PANalytical X'Pert PRO X-ray diffractometer equipped with a PIXcel solid-state detector. The samples were finally characterised using synchrotron X-ray diffraction [20].

Neutron diffraction experiments were carried out on the TOF-type diffractometer Super-HRPD installed at the Material and Life Science Facility (MLF) of the Japan Proton Accelerator Research Complex (J-PARC). A 10 g powder sample was placed in a vanadium holder (9.5 mm in diameter and 50 mm in length) and mounted in a CCR cryostat. All diffraction patterns were recorded over the time-of-flight range 17–185 ms in both the back-scattering and 90° position-sensitive detector banks, corresponding to *d*-spacings from 0.35 to 3.8°A (at a resolution $\Delta d/d \sim 4\times10^{-4}$) and from 0.75 to 5.3 A° ($\Delta d/d \sim 2 \times 10^{-3}$), respectively independent of *d*. The patterns were normalized and corrected for detector efficiency according to prior calibration with a vanadium scan. The structures were refined using the Rietveld method as implemented in the GSAS program [21]. The background and peak widths were refined together with the lattice parameters, atomic positions, and isotropic and anisotropic atomic displacement parameters (ADP) for the cations and oxygen anions, respectively.

Magnetic susceptibility and electrical resistivity were measured with a Quantum Design Physical Property Measurement System (PPMS) system in the range 5–400 K. Zero-field cooled (ZFC) and field-cooled (FC) magnetic susceptibility data were collected with a magnetic field of 100Oe, 500Oe, and 1000 Oe. The AC magnetic susceptibilities for selected samples were measured at frequencies of 10, 31.62, 100, 316.2, 1000, 3162.3, and 10000 Hz with an alternating field 10 Oe and 3 Oe respectively.

The microstructure and homogeneity of the samples was examined by scanning electron microscopy (SEM) using a Zeiss UltraPlus FE SEM**.** The average cationic composition for each sample was verified by energy dispersive spectroscopy (EDS) using the same microscope. In all cases, the measured values were consistent with the nominal compositions.

Ti and Mn K-edge XANES spectra were collected on beamline 16A1 at the National Synchrotron Radiation Research Center (NSRRC) in Hsinchu, Taiwan[22]. Finely ground samples were dispersed onto Kapton tape and placed in front of the X-ray beam at a 45$^{o}$ angle. Spectra were collected in fluorescence yield (FLY) mode using a Lytle detector. An energy step-size of 0.2 eV was used near the absorption edge. The Ti K-edge spectra were calibrated against elemental Ti with the maximum in the first derivative of the K-edge set to 4966.4 eV. The Mn K-edge spectra were calibrated against elemental Cr with the maximum in the first derivative of the K-edge set to 5989.2 eV. All XANES spectra were analysed using the Athena software program [23].

**Results and discussion**

We recently reported the results of a structural study on the La-doped system $Sr_{1-x}La_xTi_{0.5}Mn_{0.5}O_3$ [19]. In that work we showed that the structure evolves from cubic to rhombohedral as the La content was increased to 0.5. This is a reflection of changes in the tolerance factor which decreases as the La is added, from $t$ = 1.020 for $x$ = 0 to $t$ = 0.977 for $x$ = 0.5. Whilst the addition of La requires the formation of the Jahn-Teller active $Mn^{3+}$ ( $t_{2g}^3\, e_g^1$) cation these structural studies showed no evidence for a distortion of the $BO_6$ octahedra that would be indicative of a JT type distortion.

In the present work we have extended these structural studies through the use of high resolution neutron powder diffraction. Based on the results of our previous study we elected to study three compositions in the series $Sr_{1-x}La_xTi_{0.5}Mn_{0.5}O_3$, being cubic *(* $x$ = 0) rhombohedral ( $x$ = 0.4) and near the boundary of these $x$ = 0.25. The room temperature

structures of three oxides and the results of the structural refinement are summarised in Table 1.

Table 1. Crystallographic information obtained from the Rietveld refinement of the neutron diffraction patterns of $Sr_{1-x}La_xMn_{0.5}Ti_{0.5}O_3$ ($x$ = 0, 0.25, 0.4)

| $x$ | 0.0 | 0.25 | 0.40 | 0.40 |
|---|---|---|---|---|
| Temp (K) | 300 | 300 | 300 | 90 |
| Space group | $Pm\bar{3}m$ | $Pm\bar{3}m$ | $R\bar{3}c$ | *Imma* |
| a | 3.85627(10) | 3.88590(11) | 5.5136(3) | 5.50461(4) |
| b | 3.85627(10) | 3.88590(11) | 5.5136(3) | 7.76821(6) |
| c | 3.85627(10) | 3.88590(11) | 5.5136(3) | 5.53439(4) |
| α | 90 | 90 | 60.2070(2) | 90 |
| Vol | 57.346(2) | 58.678(3) | 119.076(10) | 236.66(1) |
| Sr/La z | ½ | ½ | ¼ | 0.52419(13) |
| $U_{iso}$ | 0.57(3) | 0.62(2) | 0.73 | 0.36 |
| $U_{iso}$ (Mn) | 0.18(2) | 0.16(2) | 0.34 | 0.05 |
| O1 x | ½ | ½ | -0.28408(8) | 0 |
| y | 0 | 0 | 0.78408(8) | ¼ |
| z | 0 | 0 | ¼ | -0.0058(4) |
| $U_{iso}$ | 0.61* | 1.20* | 1.31 | 3.42 |
| O2 y | | | | 0.02489(8) |
| O2 $U_{iso}$ | | | | 1.16 |
| $R_{WP}$ | 9.21 | 7.7 | 6.8 | 6.7 |
| $R_P$ | 7.0 | 6.4 | 6.7 | 6.2 |
| $\chi^2$ | 3.27 | 4.65 | 1.38 | 1.37 |
| Mn/Ti-O | 1.9281(1) | 1.9430(1) | 1.9611(1) | 1.9633(3)/1.9608(1) |
| $\Delta d^2$ | 0 | 0 | 0 | 0.000115 |
| tilt | 0 | 0 | 4.2 | 4.7 |

In $Pm\bar{3}m$ the *A* cations are at ½ ½ ½, the *B* cation at 0 0 0, and O at ½ 0 0. In $R\bar{3}c$ the *A* cations are on 2*a* sites at ¼ ¼ ¼ , the *B* cations on the 2*b* sites at 0 0 0, and the O on the 6*e* sites *x* ½-*x* ¼. In *Imma* the *A* cations are at 0 ¼ z, the *B* cation at 0 0 0, and O1 at 0 ¼ z and O2 ¼ x ¼ . * Anisotropic APD were refined. See Supporting information for details.

As reported previously our high resolution neutron diffraction data demonstrates that $SrTi_{0.5}Mn_{0.5}O_3$ adopts a cubic structure at room temperature and there is no evidence from either synchrotron X-ray or neutron diffraction for ordering of the Ti and Mn cations[19]. Pattern calculations show that our synchrotron data are of sufficient quality to identify such

ordering despite the small differences in scattering power of Ti and Mn; for example the (111) reflection that would occur near d = 4.45 Å is calculated to have ~ 1500 counts ( or 0.2% of the strongest (220) reflection near d = 2.72Å) which is some 15 times larger than the observed noise of the pattern – see figure S1 of the supporting information. $Sr_{0.75}La_{0.25}Ti_{0.5}Mn_{0.5}O_3$ adopts the same cubic structure at room temperature. The neutron diffraction pattern for the $x = 0.4$ sample was indicative of a rhombohedral structure in space group $R\bar{3}c$. The results of the Rietveld refinement for this are given in Table 1. In this rhombohedral structure the *B*-site cation is bonded to six oxygen anions at 1.96109(7) Å; this structure does not allow for a JT-type distortion associated with the $Mn^{3+}$ cation, although it is possible that locally the $Mn^{3+}$ cations may exhibit some distortion of the octahedra. The oxygen stoichiometry for the three compounds was allowed to vary during the Rietveld refinement and such refinements showed there not to be appreciable anion vacancies. The average *M*-O distance increases as the amount of the larger $Mn^{3+}$ cation increases. Consequently in the final refinement cycle the anion sites were assumed to be fully occupied. Attempts to verify the absence of anion non-stoichiometry by TGA were unsuccessful.

Cooling the two cubic oxides $SrTi_{0.5}Mn_{0.5}O_3$ and $Sr_{0.75}La_{0.25}$ $Ti_{0.5}Mn_{0.5}O_3$ to 10 K did not result in any changes to the neutron diffraction patterns that could be ascribed to either a crystallographic or magnetic phase transition. Rietveld refinements in $Pm\bar{3}m$ were successful. Conversely, cooling the rhombohedral sample $Sr_{0.60}La_{0.40}$ $Ti_{0.5}Mn_{0.5}O_3$ to 90 K resulted in a transition to an orthorhombic structure that was identified as having *Imma* space group symmetry. A $R\bar{3}c$ to *Imma* transition has been identified in a number of manganites[24, 25] and involves a first order re-orientation of the tilts from (111) to (011), and as apparent from Figure 2 there is an abrupt change in the, appropriately scaled, lattice parameters at this transition. Cooling the sample to 10K results in a number of changes in the appearance of the diffraction pattern and a satisfactory fit was obtained from a two phase model *Imma* + *I*4/*mcm*. Unfortunately it was not possible to obtain a pattern that contained only the tetragonal *I*4/*mcm* and the large errors in the refined structural parameters for this phase preclude discussion of this. It is unclear if the small discontinuity in the lattice parameters near 50 K evident in Figure 2 is significant; it may be associated with the onset of magnetic interactions seen in the susceptibility measurements as was also observed in a recent study of Pr doped $SrMnO_3$ [26].

The three structures $Pm\bar{3}m$, $R\bar{3}c$ and *Imma* are illustrated in Figure 3. The structures differ in the nature of the cooperative tilting of the corner sharing octahedra. The

archetypal cubic $Pm\bar{3}m$ structure lacks any tilts and is described as ($a^0a^0a^0$) in Glazers notation. The rhombohedral $R\bar{3}c$ structure has a single out-of-phase tilt about the $[111]_p$ directions or ($a^-a^-a^-$). The magnitude of this tilt in the x = 0.4 oxide at room temperature as estimated from the refined atomic coordinates is 4.2°. The *Imma* phase also contains a single out-of-phase tilt however this is about $[011]_p$ or ($a^0b^-b^-$). A transition from $R\bar{3}c$ to *Imma* involves a reorientation of the tilt and must be first order, although the size fo the tilt need not change dramatically through the transition , and for $Sr_{0.60}La_{0.40}$ $Ti_{0.5}Mn_{0.5}O_3$ at 90 K this is estimated to be 4.5 ° .

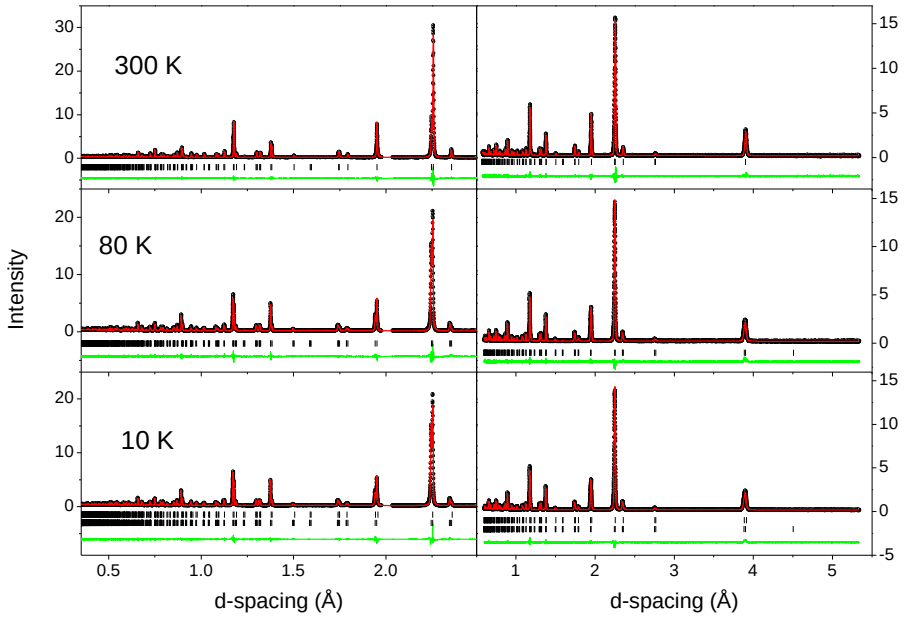


Figure 1. Observed, calculated and difference neutron diffraction profiles for $Sr_{0.60}La_{0.40}$ $Ti_{0.5}Mn_{0.5}O_3$. The left hand patterns are from the back-scattering detector bank and the right hand panels are from the 90 degree detector bank. The fits are to a rhombohedral model at 300K, orthorhombic model at 80 K and two phase orthorhombic + tetragonal model at 10 K. More detail is available in the supporting data.

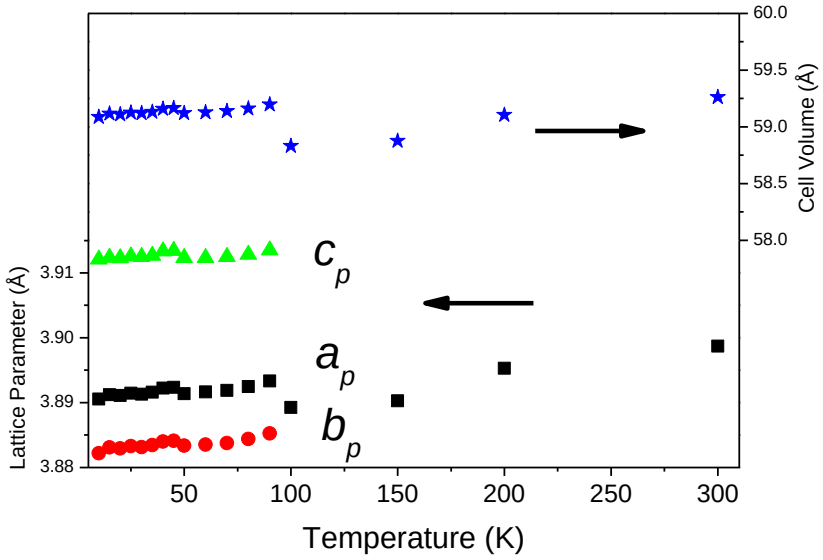


Figure 2. Temperature dependence of the appropriately scaled refined lattice parameters and unit cell volume for $Sr_{0.60}La_{0.40}$ $Ti_{0.5}Mn_{0.5}O_3$. Where not obvious the esds are smaller than the symbols. The lattice parameters were obtained from Rietveld refinements against neutron diffraction data, and only those for the orthorhombic and rhombohedral phases are illustrated. The small discontinuity in the lattice parameters around 45 K is believed to be a consequence of magnetic effects.

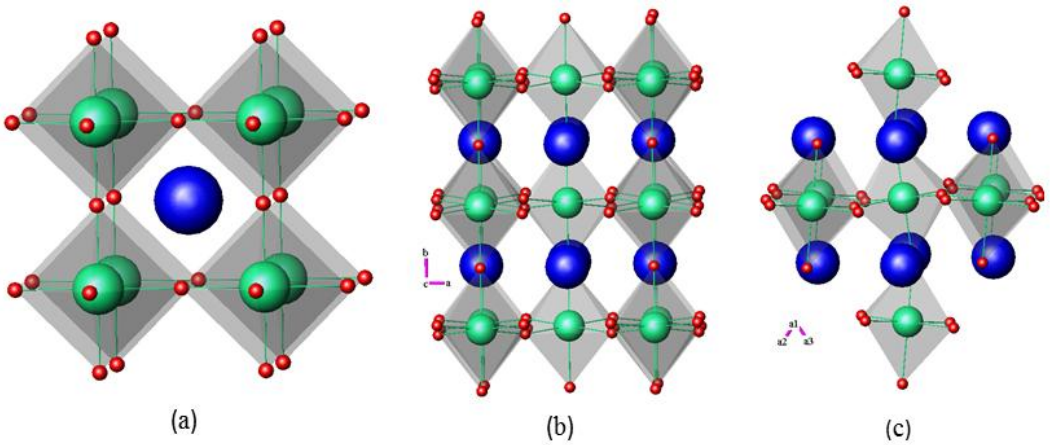


Figure 3. Representation of the structures observed in the $Sr_{1-x}La_xTi_{0.5}Mn_{0.5}O_3$ oxides (a) cubic $Pm\bar{3}m$ (b) orthorhombic *Imma*, and (c) rhombohedral $R\bar{3}c$. Note view axes are chosen to show the octahedral distortions

***XANES***

To confirm the expected valence state of Mn cations in $Sr_{1-x}La_xTi_{0.5}Mn_{0.5}O_3$, Mn K-edge XANES spectra were collected (Figure 4a). In general, first-row transition-metal K-edge XANES spectra contain two major features: a main-edge feature (feature A) and pre-edge feature (feature B)[27]. Feature A corresponds to a dipole-allowed transition of a 1s electron into empty Mn 4p states. The position of the main-edge peak, the absorption edge energy, is sensitive to the overall oxidation state of the Mn cations and is commonly used to study changes in the oxidation state of Mn cations in manganese oxides[6, 7, 28-31]. Feature B corresponds to a dipole-forbidden transition of a 1s electrons into unoccupied Mn 3d states hybridized with O 2p states. Features in the pre-edge region near the main-edge may also correspond to the transition of 1s electrons into neighbouring Mn 3d states[23] or low energy Mn 4p states[31]. The intensity and energy position of the pre-edge peak is sensitive to a number of structural and electronic features including oxidation state, coordination environment, and crystal symmetry[27, 32].

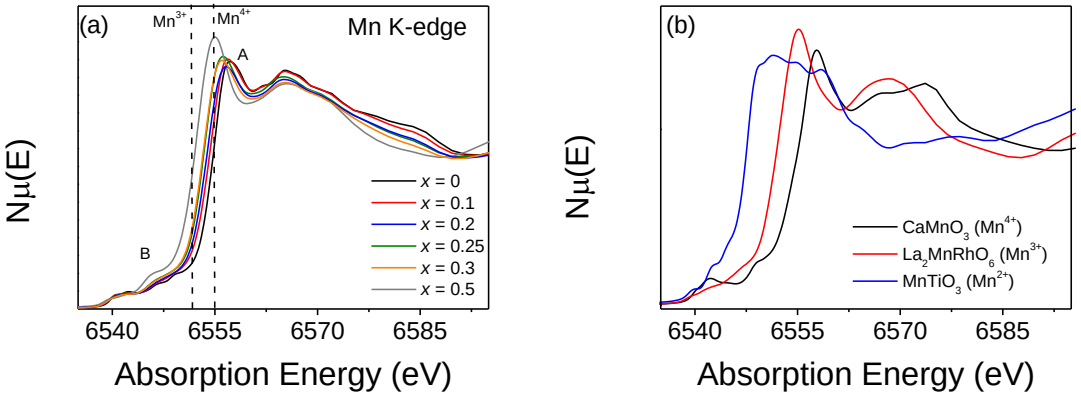


Figure 4**.** The Mn K-edge XANES spectra of (a) $Sr_{1-x}La_xMn_{0.5}Ti_{0.5}O_3$ ($x$ = 0, 0.1, 0.2, 0.25, 0.3, 0.5) and (b) standards $MnTiO_3$ ($Mn^{2+}$), $La_2MnRhO_6$ ($Mn^{3+}$), and $CaMnO_3$ ($Mn^{4+}$). The main-edge and pre-edge regions are labelled A and B, respectively. Dashed lines represent the absorption edge energy of $Mn^{3+}$ and $Mn^{4+}$ standards. All spectra were collected in florescence mode.

There is a general decrease in the Mn K-edge absorption edge energy across the $Sr_{1-x}La_xTi_{0.5}Mn_{0.5}O_3$ series with increasing $x$, consistent with a decrease in the oxidation state of the Mn cations. This decrease in oxidation state is also supported by a gradual decrease in the intensity of the pre-edge edge features (due to a decrease in unoccupied Mn 3d states with

decreasing oxidation state)[6, 7]. When compared to standards of known oxidation states (Figure 4b), the absorption edge energies of end members $SrTi_{0.5}Mn_{0.5}O_3$ (6555.1 eV) and $Sr_{0.5}La_{0.5}Ti_{0.5}Mn_{0.5}O_3$ (6552.4 eV) are [22]comparable to $CaMnO_3$ (6555.8 eV) and $LaMnRhO_6$ (6552.6 eV), respectively, suggesting that the oxidation state of Mn decreases from +4 to +3 with increasing *x*. It should be noted that no changes were observed in the Mn K-edge XANES spectra of $Sr_{1-x}Ca_xTi_{0.5}Mn_{0.5}O_3$ (See Figure S5 in Supporting Information), confirming that the Mn cations maintain a +4 oxidation state with increasing x. The composition dependence of the oxidation states of the Mn were estimated by fitting the Mn K-edge spectra with a linear combination of $La_2MnRhO_6$ ($Mn^{+3}$) and $CaMnO_3$ ($Mn^{4+}$). As shown in Figure 5, the oxidation state of Mn decreases from +3.94 to +3.04 across the $Sr_{1-x}La_xTi_{0.5}Mn_{0.5}O_3$ series. These values are consistent with the lack of detectable anion vacancies in the neutron diffraction analysis.

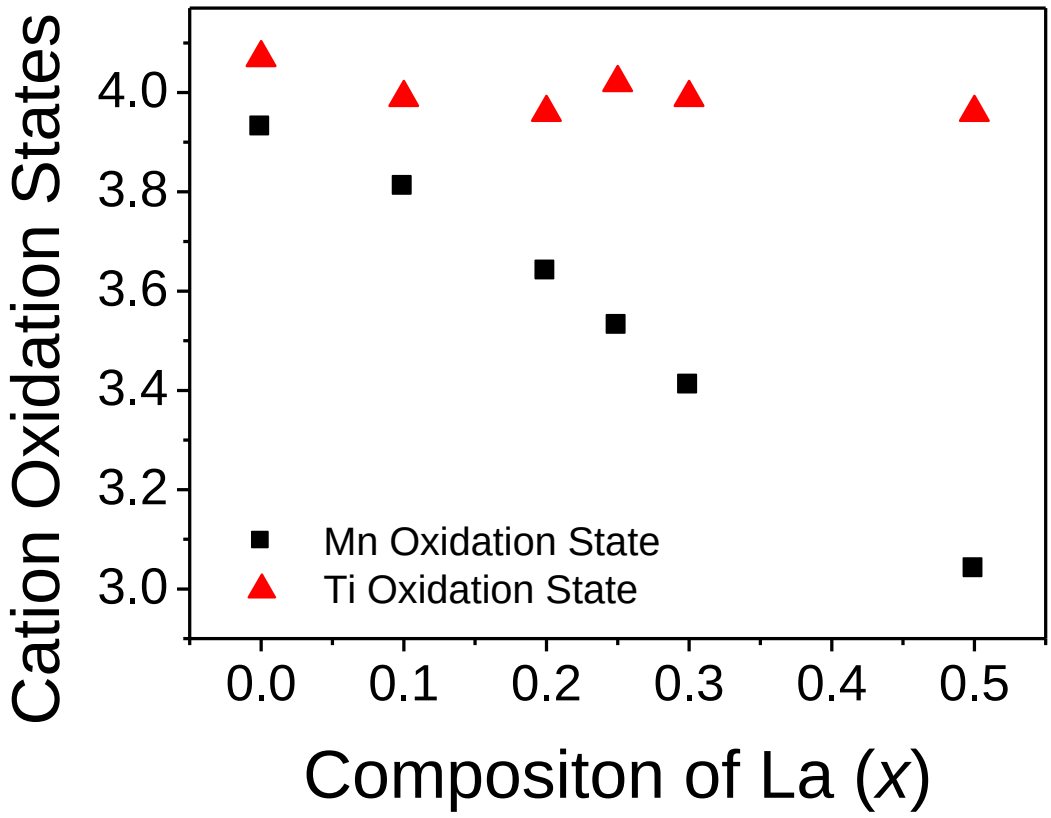


Figure 5. Variations in the oxidation states of Mn and Ti estimated from a linear combination analysis of the Mn K-edge XANES spectra using $La_2MnRhO_6$ and $CaMnO_3$ as $Mn^{3+}$ and $Mn^{4+}$ standards, respectively.

The linear combination fitting of the Mn K-edge XANES spectra implies that the oxidation state of Ti remains +4 across the series. To confirm that there are no changes in the

Ti oxidation state, Ti K-edge XANES spectra were collected (Figure 6). Unfortunately, due to a lack of appropriate $Ti^{3+}$ standards, it is not possible to determine the oxidation state of Ti *via* linear combination analysis. However, information on the oxidation state and coordination environment of Ti cations can be inferred from the Ti K-edge. Like the Mn K-edge, the Ti K-edge consists of a main-edge feature (Feature A) and a pre-edge feature (Feature B). The absorption edge energy of the Ti K-edge does not change across the $Sr_{1-x}La_xMn_{0.5}Ti_{0.5}O_3$ series, confirming that there is no change in the oxidation state of the Ti cations. Although there are no significant changes in the main-edge, there are noticeable changes in the pre-edge feature. If the oxidation state of the absorbing cation is fixed, changes in the lineshape of the pre-edge are typically due to changes in coordination environment of the absorbing cations[27, 33-36]. For titanate perovskites, in particular, the pre-edge intensity is sensitive to the displacement of $Ti^{4+}$ cations [37-40]. There are four peaks (labelled B1-B4) observed in the Ti K-edge pre-edge. Peaks B1 and B2 corresponds to the transitions of 1s electron into $t_{2g}$ and $e_g$ states, respectively [35, 38]. Due to hybridization with O 2*p* states, the $e_g$ peak is incredibly sensitive to the displacement of the Ti cations within the $TiO_6$ octahedra. In general, B1 decreases in intensity relative to B2 across the $Sr_{1-x}La_xMn_{0.5}Ti_{0.5}O_3$ series, consistent with an increase in the distortion of the $TiO_6$ octahedra expected with the $Pm\bar{3}m \rightarrow R\bar{3}C$ phase transition. The changes in peaks B3 and B4 are less obvious. Features in this region of the pre-edge are typically due to the transition of the 1*s* electron into the $t_{2g}$ (peak B3) and $e_g$ states of neighbouring $Ti^{4+}$ and $Mn^{3+}/Mn^{4+}$ cations [35, 37-40]. It is possible that the two peaks correspond to $t_{2g}$ (peak B3) and $e_g$ (peak B4) states of the neighbouring Ti/Mn cations. B4 decreases in intensity relative to B3 with increasing *x*, suggesting that there is a decrease in the number of available neighbouring $e_g$ states. This is consistent with the decrease in the oxidation stat of Mn observed in Mn K-edge (fewer empty Mn $e_g$ states). This is also consistent with the lack of lineshape changes observed in the pre-edge region of the Ti K-edge XANES spectra of $Sr_{1-x}Ca_xMn_{0.5}Ti_{0.5}O_3$ (See Figure S6 in Supporting Information) as there is no change in the $Mn^{4+}$ oxidation state across the $Sr_{1-x}Ca_xMn_{0.5}Ti_{0.5}O_3$ series.

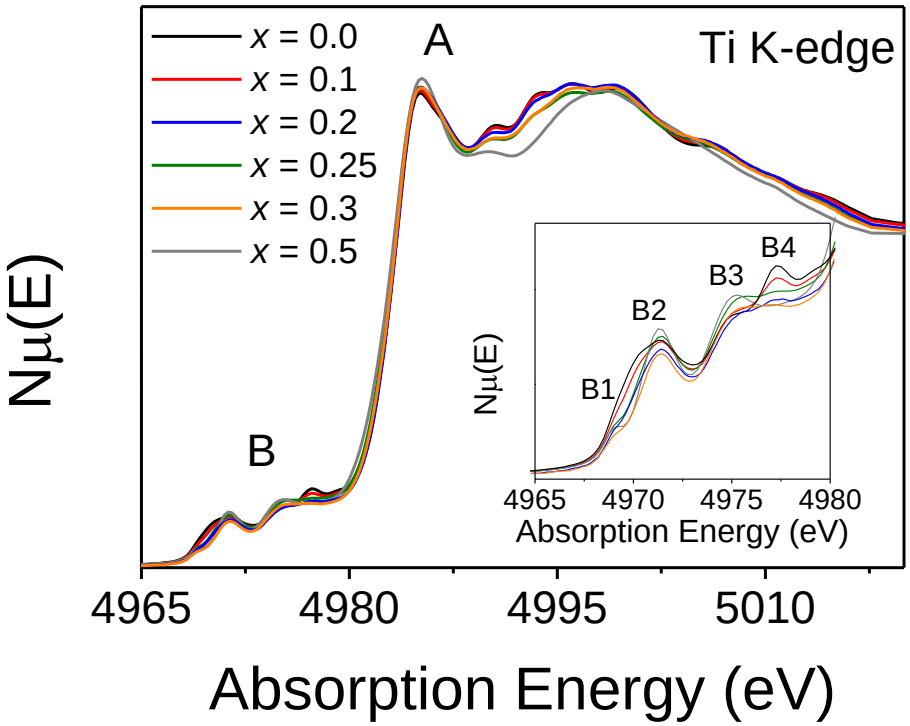


Figure 6. Ti K-edge XANES spectra of $Sr_{1-x}La_xMn_{0.5}Ti_{0.5}O_3$.(x = 0, 0.1, 0.2, 0.25, 0.3, 0.5) highlighting the main-edge (Labelled A) and pre-edge (Labelled B) regions. Insert shows the various features (labelled B1-B4) of the pre-edge. All spectra were collected in fluorescence mode.

In summary the XANES measurements confirm our expectation that the addition of $La^{3+}$ to $SrTi_{0.5}Mn_{0.5}O_3$ results in reduction of the Mn cations from $Mn^{4+}$ to $Mn^{3+}$. The data show that the local distortions of the $TiO_6$ octahedra increase with increasing La content, in agreement with evidence from our diffraction studies. Analysis of the XANES data suggests that there are no appreciable anion vacancies.

**Magnetism in $Sr_{1-x}La_xTi_{0.5}Mn_{0.5}O_3$**

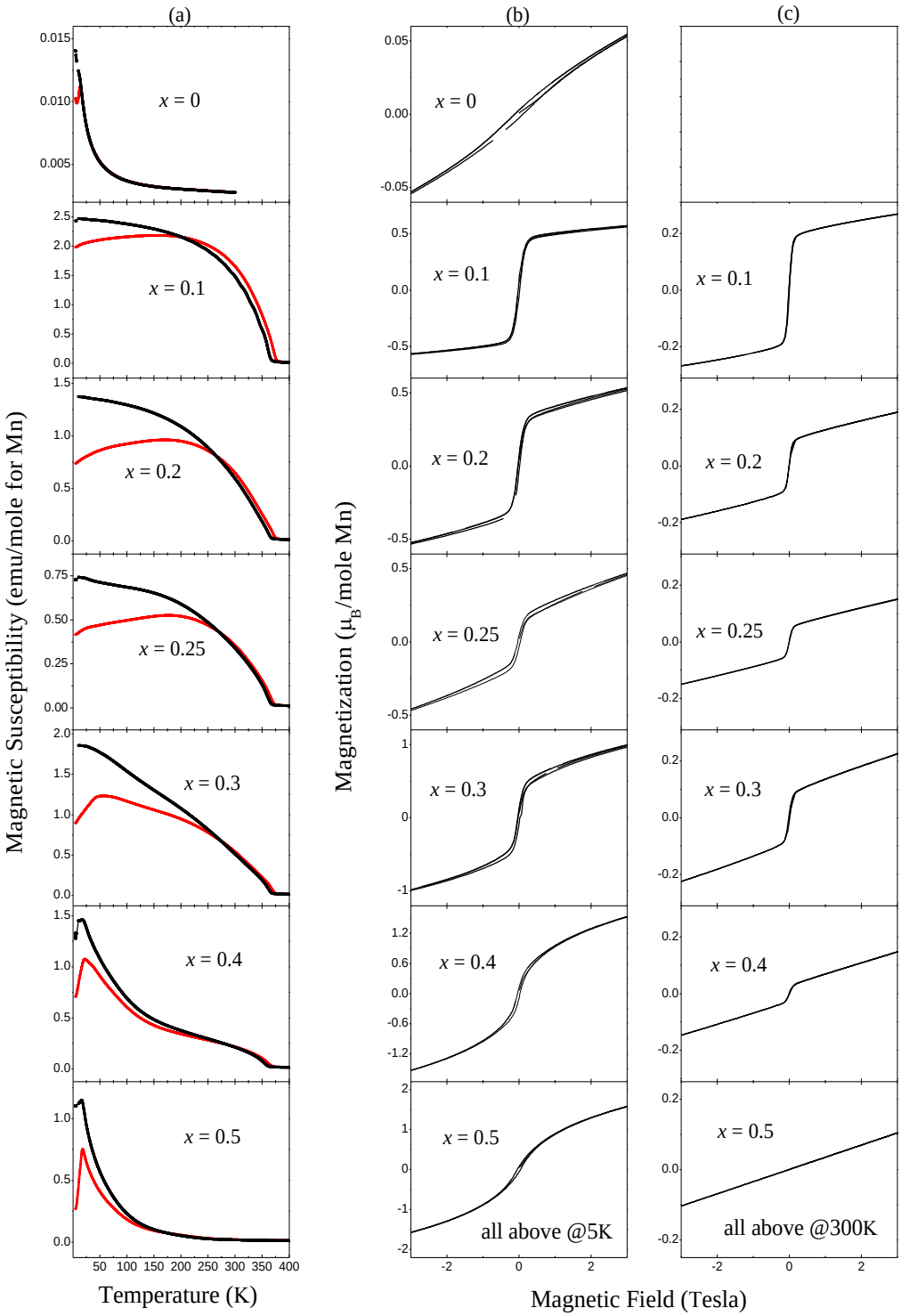


Figure 7. (a) Zero field cooled (ZFC) and field cooled (FC) Magnetic susceptibilities for $Sr_{1-x}La_xTi_{0.5}Mn_{0.5}O_3$ measured in an applied magnetic field of 100 Oe. The ZFC measurements are shown as red symbols and the FC as black symbols. M-H magnetization hysteresis loops for $Sr_{1-x}La_xTi_{0.5}Mn_{0.5}O_3$ measured at (b) 5K and (c) 300K.

The temperature dependence of the zero field-cooled (ZFC) and field-cooled (FC) magnetic susceptibilities of the various compositions studied, illustrated in Figure 7, show a remarkable sensitivity to composition. To a first approximation the magnetic structure changes from antiferromagnetic (AFM) at $x = 0$ to ferromagnetic (FM) at $x = 0.1$. Increasing the $La^{3+}$ (and hence $Mn^{3+}$) content further results in a decrease in the susceptibilities at low temperatures, indicative of AFM coupling and a general weakening of the FM exchange such that for $x = 0.5$ the AFM exchange appears to again dominant.

Ferromagnetism in manganate perovskites is generally explained by a double-exchange mechanism[41] in which an $e_g$ electron moves between the $Mn^{3+}$ and $Mn^{4+}$ cations *via* the 2*p* orbital of a bridging oxygen. Two features of the present oxides are relevant to this. Firstly the amount of $Mn^{3+}$ and hence occupancy of the $e_g$ orbitals depends on the precise composition. The importance of this is reduced as the amount of $Mn^{4+}$ decreases. Secondly the Mn and Ti are disordered at the centre of the $BO_6$ octahedra and the Ti will effectively dilute the spins; however, since Ti has empty $e_g$ orbitals it may still propagate next-nearest neighbour exchange interactions.

Antiferromagnetism in manganate perovskites is generally explained by a superexchange mechanism[42]. The antiferromagnetic superexchange interactions are likely to involve the $t_{2g}$ electrons and these interactions may be orthogonal to the ferromagnetic interactions. This has been observed in $Sr_{1-x}La_xMnO_3$.

The changes evident in Figure 7 mirror the behaviour of the analogous manganate series $Sr_{1-x}La_xMnO_3$, but are noticeably different to that seen for $Sr_{1-x}Bi_xTi_{0.5}Mn_{0.5}O_3$ which displays paramagnetic behaviour that is moderated by weak exchange coupling[13]. It was proposed that in $Sr_{1-x}Bi_xTi_{0.5}Mn_{0.5}O_3$ disorder of the Ti and Mn cations frustrates long range magnetic ordering [13]. Although the Ti and Mn cations are also disordered in $Sr_{1-x}La_xTi_{0.5}Mn_{0.5}O_3$ this does not appear to suppress short range magnetic interactions, suggesting a special role for the $Bi^{3+}$ cations. The increase in the $Mn^{3+}$ concentration that accompanies La doping in $Sr_{1-x}La_xTi_{0.5}Mn_{0.5}O_3$ is expected to enhance the ferromagnetic double-exchange interaction between the $Mn^{3+}$ and $Mn^{4+}$ ions. The data for $Sr_{1-x}La_xTi_{0.5}Mn_{0.5}O_3$ demonstrate that the co-existence of $Mn^{3+}$ and $Mn^{4+}$ is a requirement for FM behaviour and it is illustrative that this appears to be strongest at $x < 0.2$ rather than $x = 0.25$, as might have been expected, due to the 1:1 ratio of $Mn^{3+}$:$Mn^{4+}$. Recall that samples up to $x = 0.2$ are cubic (space group $Pm\bar{3}m$) but for higher $x$ values they are rhombohedral (space group $R\bar{3}C$) suggesting that the precise structure may play a role in this.

One consequence of the strong FM coupling seen for the $x$ = 0.1~ 0.4 samples is branching of the ZFC and FC susceptibility curves near 400K. Only for the $x$ = 0 and 0.5 samples did the inverse susceptibility obey the Curie-Weiss law over a reasonably large temperature range. The effective moment for the $x$ = 0 sample is estimated to be 4.66 $\mu_\beta$ which is slightly larger than the spin-only value of 3.87 $\mu_B$. This increase is possibly due to the formation of magnetic clusters giving rise to superparamagnetic behaviour. For the x = 0.5 sample the observed moment of 4.81 $\mu_B$ is in good agreement with the expect spin only value of 4.90 $\mu_B$.

The La-doped samples behave like soft ferromagnets below room temperature as evident from both the divergence of ZFC-FC susceptibilities and the field-dependence of magnetisation. They show high magnetic susceptibility with no clear saturation moment (most obvious in the 5K hysteresis loops for the $x$ = 0.1 ~0.3 samples) and extremely narrow (almost zero) coercivity. These are the key characteristics of superparamagnetic systems, such as those composed of small ferromagnetic nanoparticles. The complex magnetic behaviour is possibly influenced by grain boundary effects. Scanning Electron Micrographs (SEM) and associated elemental maps for $Sr_{0.5}La_{0.5}Ti_{0.5}Mn_{0.5}O_3$ are illustrated in Figure 8. The sample is observed to be highly crystalline and, with the exception of a build up of carbon (from the coating) at the pores, the samples appear homogeneous.

Mapping across the grain boundaries demonstrates these are rich in La and Mn (Sr-Ti poor), see Figure 8(i). It is possible that magnetism from the grain boundaries will be different to that of the bulk sample, although the volume fraction of the material in the grain boundries appears to be considerably less that that within the main particles. Further, SEM analysis of samples with lower La contents did not reveal similar effects. Since this grain boundary enrichment is only evident for the $x$ = 0.5 sample, possibly due to the 1:1 ratio of $LaMnO_3$ and $SrTiO_3$ in this particular sample, it is believed that this is not the cause of the unusual magnetic properties seen here. For lower La doped samples in the $Sr_{1-x}La_xTi_{0.5}Mn_{0.5}O_3$ series, the coexistence of $Mn^{3+}$, $Mn^{4+}$, $Ti^{4+}$ and their unequal ratio appears not to favour such phase separation. Although not immediately apparent in our SEM studies of the samples with $x < 0.5$, phase enrichment may still be present on the nanoscale and this influence the magnetic behaviour.

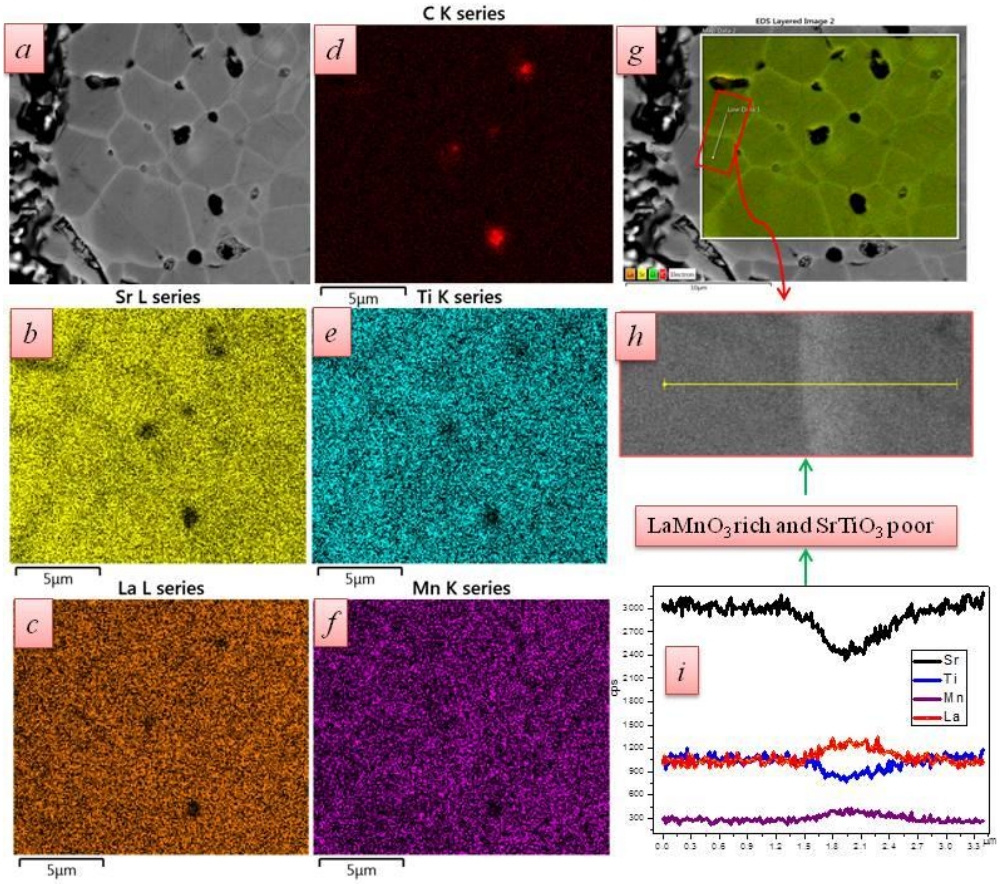


Fig. 8 SEM elemental mapping and line spectra for $Sr_{0.5}La_{0.5}Ti_{0.5}Mn_{0.5}O_3$. (a) Backscattered SEM micrograph. (b)-(f) Elemental maps. In (d) the carbon coating is found to concentrate in the pores of the sample. The results in (i) show the variation of the elements across the grain boundary illustrated in (g and h).

Whilst our results are in general agreement with those presented previously by Álvarez-Serrano[14, 16] and Kallel *et al.*[15] there are a number of small differences between them. There is now ample evidence that magnetic and orbital ordering and various modes of coupling between spin subsystem and the lattice are extremely sensitive to factors such a particle size, grain boundaries and local disorder [43]. This sensitivity is apparent when one compares ZFC-FC magnetic susceptibilities for our $x$ = 0.25 and 0.5 samples at the same magnetic field (500 Oe) which Kallel *et al.* used (See Figure S7 in Supporting Information) and we postulate that small differences in the thermal treatment of the samples employed in the various studies introduces some variation.

***Resistivity***

The temperature dependent variation of electrical resistivity in the range of 5–300 K of the various samples studied is illustrated in Figure 9 and demonstrates that all the samples are semiconductors. The conductivity of polycrystalline samples is known to be extremely sensitive to the microstructure of the sample with grain boundaries suppressing the connectivity of the samples. This is evident from the non-systematic variation in resistivity with composition evident in Figure 9. Critically the activation energy for each sample was estimated from a linear fit of ln(1/R) vs 1/T and was found to progressively increase with increasing La-doping, from 0.13eV for $x$ = 0.1 to 0.18 eV for $x$ = 0.5. This behaviour is in contrast to the metallic conductivity observed in the analogous $Sr_{1-x}La_xMnO_3$ oxides which are metallic below 300K[1]. In our case, replacement of 50% of Mn with Ti clearly precludes metallic conductivity. There is no obvious correlation between the ferromagnetic transition temperature $T_C$ and conductivity. We believe that the activation energies are influenced mainly by local structural distortion rather than FM double exchange interactions proposed by Dabrowski *et a.*l to be important in the pure manganites.[44] A detailed understanding of the composition dependence of the conductivity requires studies of single crystals and is beyond the scope of the previous work.

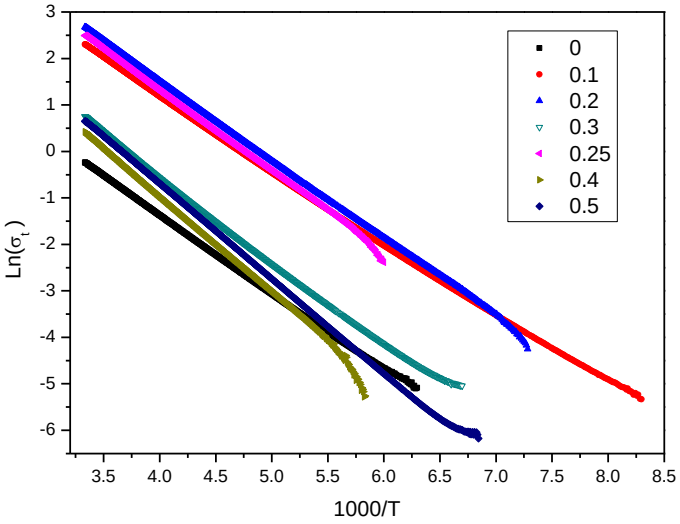


Figure 9. The Arrhenius plots of Ln (σ) verses the inverse temperature for various $Sr_{1-x}La_xTi_{0.5}Mn_{0.5}O_3$ samples. The slight curvature evident at low temperatures is an instrumental effect.

## Conclusion

The structures of the mixed metal perovskites $Sr_{1-x}La_xTi_{0.5}Mn_{0.5}O_3$ have been established using a combination of synchrotron and neutron diffraction methods and the magnetic and dc resistivity of these described. At room temperature the oxides have a cubic structure in space group $Pm\bar{3}m$ for $x \leq 0.25$ and rhombohedral in $R\bar{3}c$ for $0.3 \leq x \leq 0.50$. X-ray absorption spectroscopic measurements demonstrate the addition of $La^{3+}$ is compensated by the partial reduction of $Mn^{4+}$ to $Mn^{3+}$. Variable temperature neutron diffraction measurements show that cooling $Sr_{0.6}La_{0.4}Ti_{0.5}Mn_{0.5}O_3$ results in a first order transition from rhombohedra to an orthorhombic structure in *Imma*. The magnetic properties are shown to be extremely sensitive to the $Mn^{3+}$ content that forms as a consequence of the addition of $La^{3+}$.

The present samples are somewhat of a paradox. The structural studies demonstrate the absence of long range Ti-Mn ordering. The dc electrical resistivity measurements indicate the samples are activated semiconductors consistent with the disorder of the $Ti^{4+}$ ($d^0$) and Mn cations. This disorder is expected to frustrate magnetic ordering and the neutron diffraction measurements are in keeping with this expectation. Despite the clear evidence for

cation disorder the samples show complex magnetic behaviour indicative of robust magnetic interactions. These apparently conflicting observations suggests the formation of microdomains with short range cation ordering.

As noted in the introduction there is a lack of consensus on the magnetic properties of these oxides. We postulate that this is reflects both the importance of local or short range ordering of the cations and the sensitivity if such ordering to the precise conditions used to prepare the samples. Such sensitivity plagued early studies of the magnetic studies of mixed valence $Mn^{3+}/Mn^{4+}$ materials including $Pr_{0.5}Sr_{0.5}MnO_3$ [45], and is possibly the reason for the differences between this work and that of Álvarez-Serrano and Kallel et al[14-16]. Nevertheless it is clear that the magnetic properties can be tuned by precisely controlling $Mn^{3+}/Mn^{4+}$ ratio.

**Acknowledgments**

This work was, in part, performed at the powder diffraction beamline at the Australian Synchrotron with the assistance of Dr Helen Brand, as well as the Soft X-ray Spectroscopy beamline with the assistance of Dr. Bruce Cowie. We acknowledge the support of the Australian Research Council for this work.

**References**

1. A. Urushibara, Y. Moritomo, T. Arima, A. Asamitsu, G. Kido and Y. Tokura, *Physical Review B*, 1995, **51**, 14103-14109.
2. M. Paraskevopoulos, F. Mayr, J. Hemberger, A. Loidl, R. Heichele, D. Maurer, V. Müller, A. Mukhin and A. Balbashov, *Journal of Physics: Condensed Matter*, 2000, **12**, 3993.
3. E. Dixon, J. Hadermann and M. A. Hayward, *Chem. Mat.*, 2012, **24**, 1486-1495.
4. C. Rao, *The Journal of Physical Chemistry B*, 2000, **104**, 5877-5889.
5. J. M. D. Coey, M. Viret and S. von Molnar, *Advances in Physics*, 1999, **48**, 167-293.
6. T. Y. Tan, N. Martin, Q. D. Zhou, B. J. Kennedy, Q. F. Gu, J. A. Kimpton, Z. M. Zhang and L. Y. Jang, *Journal of Solid State Chemistry*, 2013, **201**, 115-127.
7. Z. M. Zhang, B. J. Kennedy, C. J. Howard, L. Y. Jang, K. S. Knight, M. Matsuda and M. Miyake, *Journal of Physics-Condensed Matter*, 2010, **22**, 445401.
8. Z. M. Zhang, B. J. Kennedy, C. J. Howard, M. A. Carpenter, W. Miiller, K. S. Knight, M. Matsuda and M. Miyake, *Physical Review B*, 2012, **85**, 174110.
9. S. Heyraud, P. E. R. Blanchard, S. Liu, Q. D. Zhou, B. J. Kennedy, H. E. A. Brand, A. Tadich and J. R. Hester, *Journal of Physics-Condensed Matter*, 2013, **25**, 335401.
10. T. Goto, T. Kimura, G. Lawes, A. P. Ramirez and Y. Tokura, *Physical Review Letters*, 2004, **92**, 257201.
11. I. Alvarez-Serrano, M. A. Arillo, M. Garcia-Hernandez, M. L. Lopez, C. Pico and M. L. Veiga, *Journal of the American Ceramic Society*, 2010, **93**, 2311-2319.
12. K. Meher and K. B. R. Varma, *Journal of Applied Physics*, 2009, **105**, 034113.

13. I. Alvarez-Serrano, M. L. Lopez, F. Rubio, M. Garcia-Hernandez, G. J. Cuello, C. Pico and M. L. Veiga, *Journal of Materials Chemistry*, 2012, **22**, 11826-11835.
14. I. Alvarez-Serrano, M. L. Lopez, C. Pico and M. L. Veiga, *J Phys D Appl Phys*, 2007, **40**, 3016-3023.
15. N. Kallel, N. Ihzaz, S. Kallel, A. Hagaza and M. Oumezzine, *Journal of Magnetism and Magnetic Materials*, 2009, **321**, 2285-2289.
16. I. Alvarez-Serrano, M. L. Lopez, C. Pico and M. L. Veiga, *Solid State Sci*, 2006, **8**, 37-43.
17. J. Lamsal, R. Mondal, A. Kumar, K. K. Bharathi, P. N. Santhosh, R. Nirmala, A. K. Nigam, W. B. Yelon, S. Quezado and S. K. Malik, *Journal of Applied Physics*, 2011, **109**, 07E329.
18. X. H. Sun, C. C. Wang, G. J. Wang, C. M. Lei, T. Li and L. N. Liu, *Journal of the American Ceramic Society*, 2013, **96**, 513-518.
19. I. Qasim and B. J. Kennedy, *Journal of Solid State Chemistry*, 2013, **200**, 39-42.
20. K. S. Wallwork, B. J. Kennedy and D. Wang, *AIP Conference Proceedings*, 2007, **879**, 879-882.
21. A. C. Larson and R. B. von Dreele, *General Structure Analysis System (GSAS) Los Alamos National Laboratory Report No LAUR 86-748*, 2000.
22. T.-E. Dann, S.-C. Chung, L.-J. Huang, J.-M. Juang, C.-I. Chen and K.-L. Tsang, *Journal of synchrotron radiation*, 1998, **5**, 664-666.
23. B. Ravel and M. Newville, *Journal of Synchrotron Radiation*, 2005, **12**, 537-541.
24. L. M. Rodriguez-Martinez, H. Ehrenberg and J. P. Attfield, *Journal of Solid State Chemistry*, 1999, **148**, 20-25.
25. A. Gasmi, M. Boudard, S. Zemni, F. Hippert and M. Oumezzine, *J Phys D Appl Phys*, 2009, **42**, 225408.
26. T. Y. Tan, B. J. Kennedy, Q. D. Zhou, C. D. Ling, W. Miiller, C. J. Howard, M. A. Carpenter and K. S. Knight, *Physical Review B*, 2012, **85**, 104107.
27. T. Yamamoto, *X-Ray Spectrometry*, 2008, **37**, 572-584.
28. H. Kawai, M. Nagata, H. Kageyama, H. Tukamoto and A. R. West, *Electrochimica acta*, 1999, **45**, 315-327.
29. F. Bridges, C. Booth, M. Anderson, G. Kwei, J. Neumeier, J. Snyder, J. Mitchell, J. Gardner and E. Brosha, *Physical Review B*, 2001, **63**, 214405.
30. M. Sikora, C. Kapusta, K. Knížek, Z. Jirák, C. Autret, M. Borowiec, C. Oates, V. Procházka, D. Rybicki and D. Zajac, *Physical Review B*, 2006, **73**, 094426.
31. V. Cuartero, J. Blasco, J. García, S. Lafuerza and G. Subías, *Journal of Physics: Conference Series*, 2013, **430**, 012102.
32. A. Manceau, A. I. Gorshkov and V. A. Drits, *American Mineralogist*, 1992, **77**, 1133-1143.
33. S. Matsuo, N. Sakaguchi and H. Wakita, *Analytical Sciences*, 2005, **21**, 805-809.
34. T. Hashimoto, A. Yoshiasa, M. Okube, H. Okudera and A. Nakatsuka, in *X-Ray Absorption Fine Structure-XAFS13*, eds. B. Hedman and P. Painetta, Amer Inst Physics, Melville, 2007, vol. 882, pp. 428-430.
35. D. Cabaret, A. Bordage, A. Juhin, M. Arfaoui and E. Gaudry, *Physical Chemistry Chemical Physics*, 2010, **12**, 5619-5633.
36. E. R. Aluri and A. P. Grosvenor, *Physical Chemistry Chemical Physics*, 2013, **15**, 10477-10486.
37. T. Hiratoko, A. Yoshiasa, T. Nakatani, M. Okube, A. Nakatsuka and K. Sugiyama, *Journal of synchrotron radiation*, 2013, **20**, 641-643
38. R. V. Vedrinskii, V. L. Kraizman, A. A. Novakovich, P. V. Demekhin and S. V. Urazhdin, *Journal of Physics-Condensed Matter*, 1998, **10**, 9561-9580.

39. V. Krayzman, I. Levin, J. C. Woicik, D. Yoder and D. A. Fischer, *Physical Review B*, 2006, **74**, 224104.
40. I. Levin, E. Cockayne, V. Krayzman, J. C. Woicik, S. Lee and C. A. Randall, *Physical Review B*, 2011, **83**, 094122.
41. C. Zener, *Physical Review*, 1951, **82**, 403-405.
42. P. Anderson, *Physical Review*, 1950, **79**, 350.
43. V. Markovich, I. Fita, A. Wisniewski, D. Mogilyansky, R. Puzniak, L. Titelman and G. Gorodetsky, *Journal of Applied Physics*, 2010, **108**, 063918.
44. B. Dabrowski, S. Kolesnik, O. Chmaissem, T. Maxwell, M. Avdeev, P. W. Barnes and J. D. Jorgensen, *Physical Review B*, 2005, **72**, 054428.
45. B. Raveau, A. Maignan, C. Martin and M. Hervieu, *Chem. Mat.*, 1998, **10**, 2641-2652.